# Modeling and Analysis of Anti-Icing Power of Aircraft Engine Inlet Based on Symmetric Algorithms

**Hui Peng***
**1School of Aerospace Engineering, Tsinghua University, Beijing 100084, China**
**penghui17@mails.tsinghua.edu.cn**

**Abstract: To evaluate the capability of engine inlet, inlet components and power plant anti ICER under low temperature, this paper introduces the evaluation method of anti icing system for civil aviation engine room, and analyzes the anti icing power of the aircraft intake based on the symmetric algorithm. The realizable k-cube model and wall function method are used to analyze the flow field in the inlet of an aircraft engine. Based on the analysis of the flow field of the intake port of an aircraft engine, the anti ice power of the intake port is calculated according to the heat balance relationship of the intake port surface. The symmetrical particle swarm algorithm is adopted to optimize the calculation process of inlet anti- ice power, and the particle wide area learning strategy is used to promote the calculation of inlet anti-ice power. In this way, the computational complexity is significantly reduce and the accuracy of the power analysis of the inlet anti-ice is enhanced. The simulation results show that the absolute error of the proposed method is less than 1% in 1000 iterations. Through the analysis of the surface temperature changes of the inlet deflector under different experimental conditions, it can be known that the method can effectively analyze the anti-icing power of aircraft engine inlet.**
**Key words: Symmetric Algorithm; Aircraft; Engine; Inlet; Anti-Icing Power; Modeling and Analysis**
*Tob Regul Sci.™ 2021;7(6): 6361-6374*
*DOI: doi.org/10.18001/TRS.7.6.109*

## 1 Introduction

When an aircraft is flying under icing conditions, the intake port, intake components and power devices of the engine may freeze, causing a significant impact on the engine [1]. Therefore, preventing the engine from icing is the key to ensure the flight safety of the aircraft.

Under the condition of icy weather, there are a large number of liquid supercooled water droplets in the cloud layer whose temperature is lower than 0℃. The supercooled droplets in the air have a great impact on the front lip of the intake port in the engine nacelle, and the ice will change the aerodynamic shape of the lip, reduce the intake volume and the thrust of the engine [2]. Severe problems such as compressor surge will occur, leading to the deterioration of engine performance, and the ice in the intake port will fall off and be absorbed into the engine. Accidents that may cause aircraft crashes pose a serious threat to flight safety [3].

Inlet anti-icing system is an important means to ensure the quality of engine intake flow field. The anti-icing methods of intake short cabin mainly include electric heating anti-icing and hot air anti-icing, of which the working logic is relatively simple [4],

and the system integration is relatively easy. The hot air anti-icing can be divided into dry anti-icing (full evaporation anti-icing) and wet anti-icing (semi-evaporation anti-icing).

Aircraft engine inlet icing is the most dangerous aircraft icing[5-6], which directly leads to the damage of the aerodynamic appearance of the inlet, reduces the thrust of the engine [7] and increases the flight load. Moreover, when the ice layer in the inlet falls off, it will enter the engine with the airflow, injure the fan blades with large rotational speed, and cause mechanical damage to the compressor, even to the whole engine. Engine damage [8] directly causes flight accidents. To ensure flight safety, airworthiness clauses put forward relevant safety requirements for engine inlet anti-icing. At present, hot air from engine compressor is mostly adopted as the heat source of engine inlet anti-icing. Hot air enters into the anti-icing pipeline at the front of the inlet. The hot air redistribution [9] plays an anti-icing role through the role of flute tube orifice.

The definition of anti-icing power requirement extracted from the hot air in the intake port directly affects the exhaust power of the engine high-pressure compressor and the performance of the high-pressure compressor [10]. The ice-proof air-entrainment power needs to be defined in the early design stage, and optimized iteratively in the conceptual stage of civil aero-engine design.

Electric anti-icing is an efficient and energy-saving deicing method, which consists of power supply device, programmer and inductor. The electric ice cutter first divides the ice into small pieces of ice, and the pulse generator generates electric pulse, which acts on the sensor, making the skin produce a pulse with short action time, and generating small amplitude and high frequency vibration. Consequently, the ice will fall off and removed quickly. The programmer is used to control the connection sequence and time of each sensor. There is a wide range of working temperature suitable for the electric anti-icing system, and its energy consumption is only 1% ~ 2% of that of the electric anti-icing system. Electric anti-icing may become the next generation of aircraft deicing system.

Although a lot of research has been carried out on the mechanism and method of ice-proof, the calculation method of anti-icing power for intake port has not been systematically studied [11]. There have been relevant literatures on the type of anti-icing system, the impact of water droplets on the wing and local water harvesting. The engineering calculation method of aggregation is introduced, but the calculation method of the anti-icing power of the intake port of Civil Aeroengine has not been systematically introduced.

M. Papadakis et al. used experimental and numerical methods to reveal the impact of the distribution angle of the orifice on the anti-icing performance; J. M. Brown et al. carried out experiments to study the distance between orifices, the distance between the orifice and the skin, the size of the orifice and the efficiency of the anti-icing system, and gave the scope of design reference; D. Rigby paid more attention to the influence of the orifice distribution configuration on the anti-icing system in the design. It was found that the efficiency of asymmetrically distributed orifices was higher. A. F. Massardo et al. put forward a new structure of the anti-icing chamber, which can save the amount of hot gas and enhance the anti-icing system efficiency. In China, Chang Shinan and QiuXigang have carried out extensive research on the performance and anti-icing effect of direct injection, chord double skin and micro-ejector structures of anti-icing chambers, obtaining a deeper understanding of the heat transfer characteristics of various anti-icing structures. In the study of flute anti-icing system, Bo Xueqin and Lin Guiping carried out numerical research on the influence of parameters such as orifice diameter, orifice number and orifice

spacing on the thermal efficiency of flute anti-icing system. Based on a certain aircraft engine, Zhu Yongfeng et al. designed a new method according to the ice swallowing ability of the engine and used it to calculate the heat flow required by the nacelle anti ice system under severe working conditions, which effectively optimized the system performance and improved the system efficiency.

In this paper, the anti-icing power of the aircraft engine inlet is modeled and analyzed based on symmetric algorithm. Based on the analysis of the flow field of the intake port of an aircraft engine, the anti ice power of the intake port is calculated according to the heat balance relationship of the intake port surface. The symmetrical particle swarm optimization algorithm is adopted to optimize the calculation process of inlet anti ice power, and the particle wide area learning strategy is used to promote the calculation of inlet anti ice power. In this way, the computational complexity is reduced and the accuracy of the power analysis of the inlet anti ice is enhanced.

## 2 Materials and methods

### 2.1 Aircraft engine inlet flow field analysis

The model mainly includes the flow equations of the cone throttle valve and the orifice, the differential equations of temperature and pressure in the pressure regulating chamber, the motion equations of the pressure stabilizing valve assembly and the cone plug. Based on the knowledge of aerodynamics, engineering thermodynamics and theoretical mechanics, the mathematical model of each component is established. The opening system with the mass flow exchanging function changes the pressure and temperature of the cavity as the air enters and exits the cavity. It is assumed that there is no heat exchange between the cavity and the outside, and the temperature and pressure in the cavity are uniformly distributed all the time.

In order to design the anti-ice system of civil aviation engine intake, the intake flow field is analyzed. In Cartesian coordinate system, the N-S control equation is shown as follows when the compressible flow in the intake port of an aircraft engine is expressed in tensor form.

(1) Continuous equation

$$\frac{\partial \rho}{\partial t}+\frac{\partial}{\partial x_i}\left(\rho u_i\right)=0 \tag{1}$$

(2) Momentum equation

$$\frac{\partial}{\partial t}\left(\rho u_i\right)+\frac{\partial}{\partial x_j}\left(\rho \overline{u_i u_j}\right)=-\frac{\partial p}{\partial x_i}+\frac{\partial}{\partial x_j}\left(\tau_{ij}-\rho u_i u_j\right), i=1,2,3$$

(2)

$u_i$ is the throttling coefficient, $u_j$ is the flow coefficient, $\rho$ is the gas density. According to the Boussinesq eddy viscous assumption, the relationship between Reynolds stress $-\rho\overline{u_i u_j}$ and velocity gradient of mean motion is established as follows:

$$-\rho\overline{u_i u_j}=\mu_t\left(\frac{\partial u_i}{\partial x_j}+\frac{\partial u_j}{\partial x_i}\right)-\frac{2}{3}\left(\rho k+\mu_t\frac{\partial u_k}{\partial x_k}\right)\delta_{ij}$$

(3)

(3) Energy equation

$$-\rho\overline{u_i u_j}=\mu_t\left(\frac{\partial u_i}{\partial x_j}+\frac{\partial u_j}{\partial x_i}\right)-\frac{2}{3}\left(\rho k+\mu_t\frac{\partial u_k}{\partial x_k}\right)\delta_{ij}$$

$$\frac{\partial}{\partial \tau}\left(\rho E\right)+\frac{\partial}{\partial x_j}\left(\rho u_i E\right)=\frac{\partial}{\partial x_i}\left\{\lambda_{eff}\frac{\partial T}{\partial x_i}-p u_i+u_j\left(\tau_{ij}\right)_{eff}\right\}$$

(4)

Total energy $E=h-\frac{p}{\rho}+\frac{1}{2}u_k u_k$, gas enthalpy $h=C_p T$.

The definitions of quantities in the formula are as follows:

$$\tau_{ij} = 2\mu\iota\left\{ S_{ij} - \frac{1}{3}\frac{\partial u_k}{\partial x_k}\delta_{ij} \right\}$$

(5)

$$S_{ij} = \frac{1}{2}\left[ \frac{\partial u_i}{\partial x_j} + \frac{\partial u_j}{\partial x_i} \right] \quad (6)$$

$$\left(\tau_{ij}\right)_{eff} = 2\mu_{eff}\left\{ S_{ij} - \frac{1}{3}\frac{\partial u_k}{\partial x_k}\delta_{ij} \right\}$$

(7)

$$\mu_{eff} = \mu_l \mu_t \quad (8)$$

$$\lambda_{eff} = \lambda_l + \lambda_t \quad (9)$$

$$\lambda_t = \frac{C_p \mu_t}{\mathrm{Pr}_t} \quad (10)$$

Where $\mathrm{Pr}_t$ is the ideal gas constant, $x_j$ is the constant entropy index, $\lambda_t$ and $\lambda_t$ are laminar and turbulent thermal conductivity, respectively, $\mu_t$ and $\mu_t$ are laminar and turbulent viscous coefficients, respectively, Prt is Prandl number of turbulent flow.

By using the method of realizable k-cube model and wall function, the complete turbulent zone is connected with the wall function [12-13], which can avoid the existence of the wall and modify the turbulent model, as shown in Figure 1.

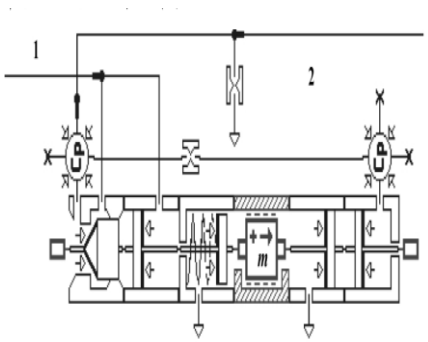


**Figure 1 System model design**

The designed model is effective for the flow with the characteristics of rotation, strong pressure gradient, separation and reflux. Its transport equation is:

$$\rho\frac{Dk}{Dt} = \frac{\partial}{\partial x_i}\left\{ \left( \mu_I + \frac{\mu_t}{\sigma_k} \right)\frac{\partial k}{\partial x_i} \right\} + G_k + G_b - \rho\varepsilon - Y_M$$

(11)

$$\rho\frac{D\varepsilon}{Dt} = \frac{\partial}{\partial x_i}\left\{ \left( \mu_I + \frac{\mu_t}{\sigma_k} \right)\frac{\partial \varepsilon}{\partial x_i} \right\} + \rho C_1 S_\varepsilon - \rho C_2 \frac{\varepsilon^2}{k + \sqrt{v\varepsilon}} + C_{1\varepsilon}\frac{\varepsilon}{k} G_{3\varepsilon} G_b \rho$$

(12)

The relevant quantities in the equation are defined as follows: $G_k$ represents the contribution of average velocity gradient to turbulent energy generation, $G_b$ represents the contribution of buoyancy to turbulent energy generation. In this paper, gravity is not taken into account, and this is omitted. $Y_M$ represents the contribution of the fluctuating expansion of compressible flow to the total dissipation rate. Sarkar proposed the following model for this term: $Y_M = \rho\varepsilon 2M_t^2$. The turbulent $M_t$ number in the formula is defined as $M_t = \sqrt{k/a^2}$ and $a$ as sound speed. $\sigma_k$ and $\sigma_\varepsilon$ are turbulent Prandtl numbers $k$ and $\varepsilon$, respectively.

$$C_1 = \max\left[ 0.43, \frac{\eta}{\eta + 5} \right], \quad \eta = Sk/\varepsilon,$$

$C_2$ and $C_{1\varepsilon}$ are model constants.

The turbulent viscous coefficient (eddy viscosity) model of the realk-ε model is $\mu_t = \rho C_\mu \frac{k_2}{\varepsilon}$.

Model constants: $C_{1\varepsilon}=1.44$ , $C_2=1.9$, $\sigma_\varepsilon$=1.0, $\sigma_k$=1.2.

At this point, the coefficient $C_\mu$ in the eddy viscosity formula of the real k-ε model is no longer a constant, but is calculated according to the following formula:

$$C_\mu=\frac{1}{A_0+A_s\frac{U^*k}{\varepsilon}} \quad (13)$$

$$U^*=\sqrt{S_{ij}S_{ij}+G_bG_k} \quad (14)$$

Where,

$$G_b=G_k-2e_{ijk}\omega_k, A_O=4.04, A_s=\sqrt{6}\cos\phi \quad (15)$$

$$G_k=\frac{1}{2}\left(\frac{\partial u_j}{\partial x_i}-\frac{\partial u_i}{\partial x_j}\right) \quad (16)$$

$$\phi=\frac{1}{3}\arccos\left(\sqrt{6}W\right) \quad (17)$$

$$W=\frac{S_{ij}S_{jk}S_{ki}}{S} \quad (18)$$

$$S=\sqrt{S_{ij}S_{ij}} \quad (19)$$

$\omega_k$ is the rotational angular velocity of the system.

Obviously, $C_\mu$ is an angular velocity function of average strain rate and rotation rate, turbulent motion and system rotation. In the inertial bottom of the equilibrium boundary layer, the value becomes 0.09.

The average velocity wall law based on Launder and Palding is as follows:

$$U^*=\frac{1}{\kappa}\ln\left(E_y{}^*\right) \quad (20)$$

Where, $U^*=\frac{U_pC_\mu^{1/4}k_p^{1/2}}{\tau_w/\rho}$ , $y^*=\frac{PC_\mu^{1/4}k_p^{1/2}y_\rho}{\mu}$。

Where, Von Karman constant $k=0.42$. $E$ is an empirical constant with a value of 9.81. $U_p$ is the average velocity of the fluid at point P. $K_p$ is the turbulent energy at point P and $Y_p$ is the distance from point P to the wall. In theory, the above logarithmic law of average velocity works only when $y^*\geq 30\sim 60$ is used; however, in practical calculation and analysis, $y^*\geq 11.225$ is generally used. When $y^*\leq 11.225$, that is, in the area close to the wall, there is $U^*=y^*$.

## 2.2 Calculation of anti-icing power of inlet port

In the calculation of the anti-icing power of the inlet surface, the energy balance neglects the change of energy in the control volume and the energy lost due to water overflow [14], and the heating effect caused by the air friction surface [15]. According to the heat balance on the surface of the intake port, the energy $\dot{Q}_{anti}$ needed for the surface of the anti-icing system should be taken into account, including the heat $\dot{Q}_{eavp}$ needed for evaporation of water on the surface, the heat $\dot{Q}_\beta$ of water droplets on the surface of the intake port, the heat $\dot{Q}_{conv}$ carried by

convective heat transfer between the airflow and the surface, and the sum of the radiation heat $\dot{Q}_{rad}$ from the anti-icing surface to the atmosphere.

$$\dot{Q}_{anti} = \dot{Q}_{eavp} + \dot{Q}_{\beta} + \dot{Q}_{conv} + \dot{Q}_{rad} \quad (21)$$

The power required for anti-icing can be expressed as follows:

$$q_{anti} = m_{evap} \cdot L_{evap} + c_h \cdot \left(T_f - T_{rec}\right) + \beta \cdot LWC_{\infty} \cdot V_{\infty} \cdot \left[\frac{\|V_d\|^2}{2} + c_p \Delta T_{\infty}\right] + \sigma\varepsilon^4 \left(T_f^4 - T_{\infty}^4\right) \quad (22)$$

Where, $m_{evap}$ is evaporation mass flow of the aircraft inlet, $T_f$ is aircraft engine anti-ice surface temperature, $\beta$ is water collection coefficient, $T_{rec}$ is boundary layer outer boundary temperature, $V_{\infty}$ is inlet flow rate, $V_d$ is far-field inflow velocity, $\Delta T_{\infty}$ is the difference between inlet temperature and engine surface temperature. Formula (22) shows that the anti-icing power is related to working parameters and surface temperature [16].

**2.3Symmetric particle swarm optimization**

The principle of symmetry is Nott's theorem. Nott's theorem is very useful because it links symmetry with conservation. It means that for every continuous symmetric transformation of a mechanical system, there is a conserved quantity corresponding to it. Symmetric particle swarm is adopted to optimize the calculation process of the inlet anti-icing power, which can effectively reduce the computational complexity and improve the accuracy of the analysis of the inlet anti-icing power. When the static particle $s$ detects the environmental changes in a region, it generates heuristic information for the real population particles, which makes each particle move towards the region, as shown in formula (23). However, in order to avoid the simultaneous changes of multiple regions, the problem of insufficient search for other regions [17] causes the real population particles to move towards the region where $s$ is located. The generated symmetrical particles are used to expand the search area in response to changes in multiple areas [18].

$$x_{ij}(t) = x_{ij}(t) + \left(x_{is}(t) - x_{ij}(t)\right) rand(0,1) \quad (23)$$

$\left(x_{is}(t) - x_{ij}(t)\right) rand(0,1)$ indicates that the real particle $j$ moves towards the region where the static particle $s$ is located. Although the possibility of falling into local optimum can be greatly reduced by using symmetrical particle tracing method, it is still possible to fall into local optimum [19]. In this paper, a particle wide area learning strategy is proposed to accelerate the population and escape from the local optimum.

By taking the current particle $k$ as the center of the circle and $r_k$ as the radiu, a circle (called neighborhood) is drawn, then the optimal particle $LB$ in the neighborhood except $k$ is obtained. The current global optimal particle is $GB$, the center point between $LB$ and $GB$ is $O$.

Particle $k$ is the inspiration information in learning $LB$ and $GB$. In order to jump out of the local optimum, it is necessary to expand its learning scope and learn from the symmetric point $SK$ with $O$ as the center in the learning process, as shown in Figure 1.

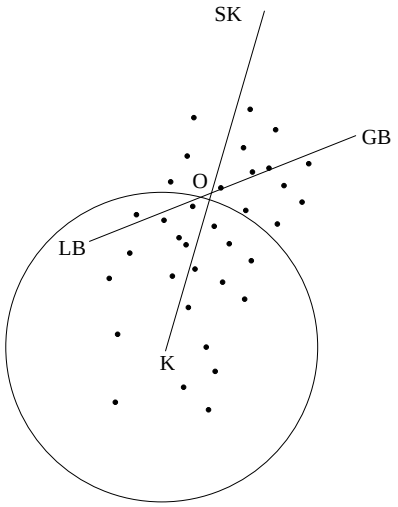


**Figure 2 Wide area learning icon**

The concrete realization is as follows:

(1) Change the speed update formula

When trapped in local optimum, the velocity update formula is changed to:

$$v_{ij}(t+1) = w \cdot v_{ij}(t) + c_1 \cdot r_1 \cdot \left( pbest_{ij}(t) - x_{ij}(t) \right) + c_2 \cdot r_2 \cdot \left( gbest_i(t) - x_{ij}(t) \right) + c_3 \cdot r_3 \cdot \left( gbest_i(t) - lbest_{ij}(t) \right) \quad (24)$$

Among them, $c_3 \cdot r_3 \cdot \left( gbest_i(t) - lbest_{ij}(t) \right)$ denotes that the particle learns from the location of $SK$; $c_3$ is a learning factor, indicating the degree of wide-area learning, in which $c_3$ takes the algebraic SNC whose optimal solution changes stagnately; $r_3$ denotes the random disturbance in the learning process, which generally takes the random number in(0,1).

(2) Disturbing the direction of later motion

After the particle $K$ moves towards $SK$, a reverse perturbation is added to the original velocity direction to keep the randomness of the particle motion direction and reduce the probability of falling into the local optimum again.

Two-Subgroup method is to expand the search scope by the mutual cooperation between two groups of main and auxiliary subgroups with opposite search direction, learn from the hybrid mechanism of genetic algorithm, and adopt the nonlinear decreasing strategy[20] of inertia weight to reduce the risk of falling into local extremum.

Symmetric particle swarm optimization (SymPSO) is described as follows:

Step1 initialize the position and velocity of the particle, calculate the fitness value, take the initial position of the particle as the best position of the individual, and choose the best position of the particle as the global best position.

Step2 initialize the position of static particles and calculates the fitness value, and guarantee the uniformity of static particle distribution by using population entropy.

Step3 execute Step8 if the convergence condition of the algorithm is satisfied; otherwise, Step4 is executed.

Step4 recalculate the fitness of each static particle and compare the current fitness with the recalculated fitness. If it is not equal, the environment changes and

Step5 is executed; otherwise, Step6 is executed.

Step5 update the position of the real population by formula(23), generate symmetrical particles for each particle, and replace the original particle with the optimal particle to enter the real population.

Step6 calculate the fitness of each particle.

Step7 If the optimal solution stagnation algebra of Step7 reaches 50, it indicates that the population may fall into local optimum. Using formula(24) to update the particle speed and increase the perturbation, it is possible to jump out of local optimum; otherwise, Step8 is executed.

Step8 If the convergence condition of the algorithm (whether the maximum number of iterations is reached) is satisfied, Step8 runs to the end; otherwise, Step3 is executed.

## 3 Results

### 3.1 Simulation experiment 1

In order to effectively monitor the effectiveness of the modeling and analysis of the anti-icing power of the aircraft engine intake port based on symmetry algorithm, the anti-icing experiments under different air velocity, different air temperature and different liquid water content were carried out on the MATLAB simulation platform. In the experiment, the inlet temperature of the anti-icing hot air is 253 degrees Celsius, the inlet pressure is 197 kPa, the flow rate is 64.5 kg/h and the diameter of water droplets is 10 microns. The power of the aircraft engine inlet under different conditions is obtained by using the proposed method, as shown in Table 1.

**Table 1 Experimental status**

| status | Air temperature/℃ | Air flow rate/m/s | Hot gas temperature/℃ | Hot air pressure/kPa | Hot gas flow/kg/h | Power / W |
|---|---|---|---|---|---|---|
| Low speed low temperature no water | -20.17 | 22.98 | 256.18 | 302.89 | 66.25 | 25614 |
| Low speed low temperature water | -20.19 | 22.98 | 254.63 | 298.79 | 65.63 | 24152 |
| Low speed high temperature no water | -5.61 | 27.16 | 256.11 | 294.62 | 64.52 | 25581 |
| Low speed high temperature water | -5.91 | 27.16 | 254.69 | 298.82 | 65.41 | 24235 |
| Medium speed low temperature no water | -17.16 | 57.18 | 252.81 | 297.11 | 65.71 | 21584 |
| Medium speed low temperature water | -17.82 | 57.18 | 255.52 | 298.82 | 65.65 | 25504 |
| Medium speed high temperature no water | -5.87 | 61.41 | 254.97 | 298.52 | 65.65 | 24851 |
| Medium speed high temperature water | -5.83 | 61.41 | 255.31 | 296.37 | 64.88 | 25205 |
| High speed and high temperature no water | -7.77 | 79.21 | 256.42 | 298.23 | 65.51 | 25836 |
| High speed and high temperature water | -5.63 | 79.21 | 253.47 | 302.41 | 66.72 | 22253 |

In Table 1, the low, medium and high velocities indicate the velocity of the airflow; the low and high temperatures indicate the temperature of the airflow; and the anhydrous and water indicates the presence or absence of supercooled water droplets in the airflow. From Table 1, it can be seen that the ice-proof power of aircraft engine inlet under different conditions can be obtained by using the proposed method.

At 0-1000 iterations, the fitness values and absolute error changes of aircraft engine inlet anti-icing power under different conditions are obtained by using the proposed method. The result of the proposed method is compared with that of the adaptive particle swarm optimization method and that of the Two-Subgroup method. The comparison results are shown in Figure 2 and 3.

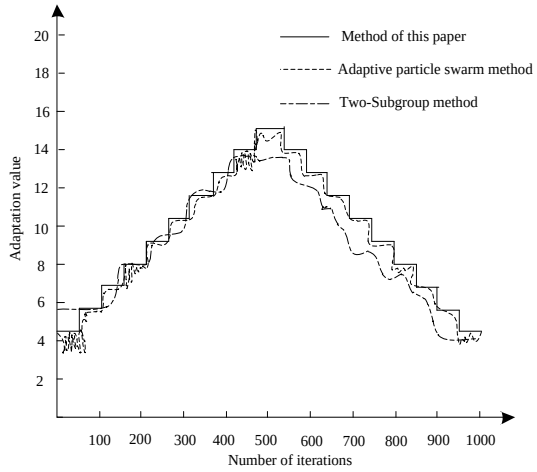


**Figure 3 Tracking extreme value changes**

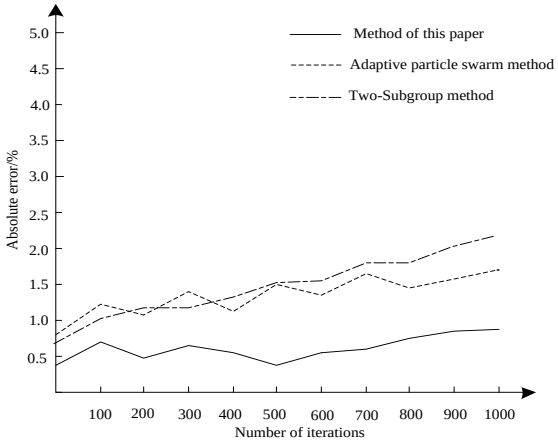


**Figure 4 Absolute error changes**

It can be seen from Figure 3 that the adaptive value of the proposed method shows stable regular change (after the number of iterations reaches 500, the adaptive value decreases regularly). Compared with the other two methods, the proposed method is more stable and shows higher adaptive value. As can be seen from Figure 4, compared with the other two methods, the proposed method has lower error.

By comparing the results of Figure 3 and 4, it can be seen that the tracking response speed of the anti-icing power of the aircraft engine inlet under different conditions is faster and the optimization error is obviously smaller than that of the other two methods. The absolute error is less than 1% when the number of iterations of the anti-icing power of the aircraft engine inlet is less than 1000. The absolute error of the anti-icing power of the aircraft engine inlet is more than 1.5% when the number of iterations is less than 1000. This shows that the proposed method can track the optimal solution at the fastest speed. The effectiveness of this method in analyzing the anti-icing power of aircraft engine intake ports under different conditions is verified.

Using the proposed method, considering the influence of the intake port at the front of the aeroengine on the icing parameters, the distribution characteristics of the flow field at the outlet of the intake port are obtained. The anti-ice ability of the air intake of aircraft engine under the condition of low speed and high temperature and under the condition of low speed and low temperature is compared and analyzed, as shown in Figure 5.

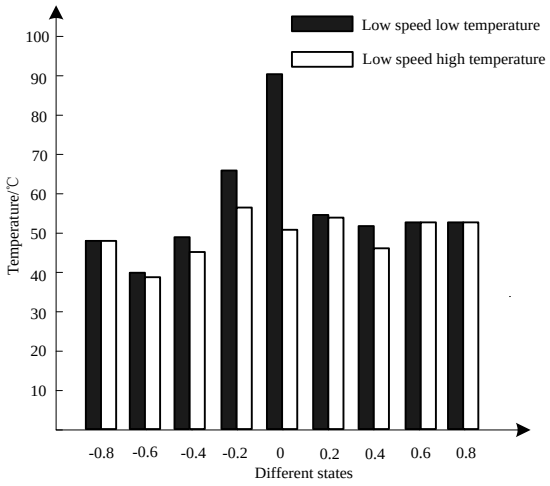


**Figure 5 Comparison of skin surface temperature with low water temperature and low temperature low temperature**

As shown in Figure 5, although the temperature distribution at low speed and high temperature is similar to that at low speed and low temperature without supercooled water droplets, the liquid water content in supercooled water droplets at low speed and high temperature is nearly twice as high as that in supercooled water droplets at low speed and low temperature, which makes the skin temperature entanglement on the central surface of the passage drop considerably, especially in droplet impact comparison. The dense frontier stagnation area declined significantly.

The proposed method is used to compare and analyze the anti-ice ability of the air intake of the aircraft engine under the condition of medium speed high temperature and under the condition of medium speed low temperature. The results are shown in Figure 6.

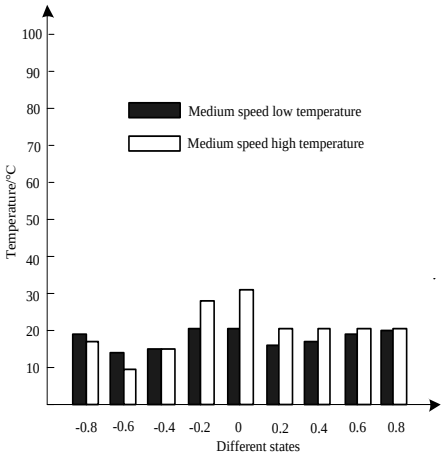


**Figure 6 Speed skin surface temperature comparisons**

As shown in Figure 6, under the same air velocity and temperature, the skin temperature at the center of the channel decreases to a certain extent because of the high liquid water content in the medium-speed and high-temperature supercooled water droplets, especially at the front stagnation point where the impact of water droplets is more intensive.

In this work, the proposed method is adopted to analyze the change of skin temperature in high temperature and anhydrous condition at different flow velocities when the anti-icing power of the aircraft engine inlet is in different states. The results are shown in Figure 7.

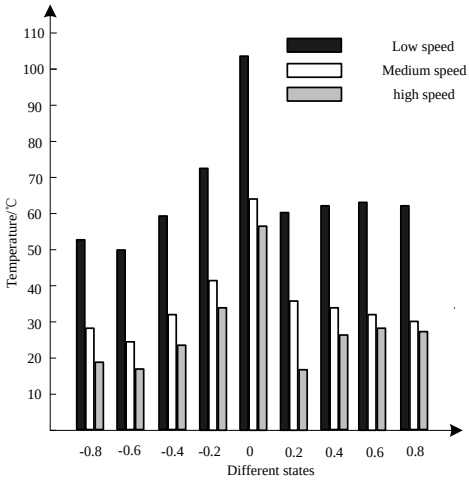


**Figure 7 Change of surface skin temperature in high temperature and no water state**

In this work, the proposed method is adopted to analyze the change of skin

temperature in high temperature and water state at different flow velocities when the anti-icing power of the aircraft engine inlet is in different states. The results are shown in Figure 8.

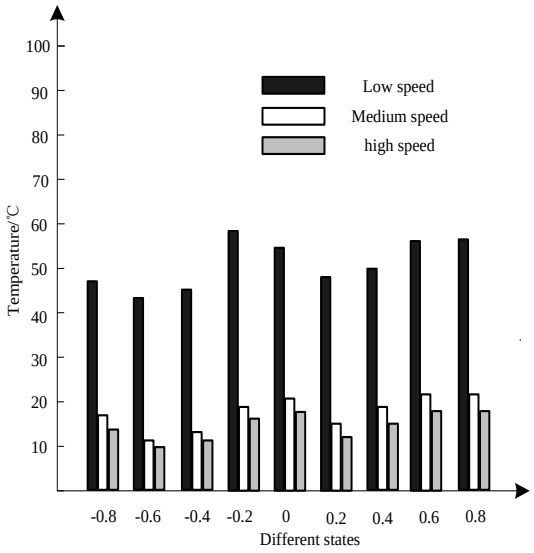


**Figure 8 Change of surface skin temperature in high temperature and water state**

As shown in Figure 7 and 8, the skin temperature at the center of the channel generally decreases significantly with the increase of air velocity. In the absence of supercooled water droplets, the surface skin temperature is relatively high because of the heat transfer enhancement effect of impinging jet in the front stagnation area. In the presence of supercooled water droplets, the temperature of the skin decreases obviously because of the dense impact of the supercooled water droplets in the front stagnation point area, which makes the surface temperature distribute uniformly along the chord direction of the whole diversion baffle.

### 3.2 Simulation experiment 2

The simulation parameters are as follows: atmospheric ambient pressure is 101325 Pa, flight Mach number is 0.4, flight angle of attack is 3°, average diameter of supercooled water drop is 20μm, liquid water content (LWC) is 1 g/m$^3$. Two sets are set up to verify the ice-proof modeling ability of inlet under different conditions.

Table 2 Parameters for calculation

| case | Environment temperature/K | Icing time/s | Inlet exit mass flow/(kg/s) |
|---|---|---|---|
| 1 | 245 | 410 | 210 |
| 2 | 255 | 410 | 210 |

Figure 9 shows the local water collection coefficient at the lip of the engine inlet. It is clear that the water droplet impact area of the inlet is concentrated near the leading edge, where there is a large velocity gradient of the air flow field, the water droplet deviates from the air flow field far away, and it is more likely to hit the engine surface. On both sides of the maximum value, the collection coefficient decreases gradually, then enters the water droplet shelter area, and the collection coefficient becomes 0.

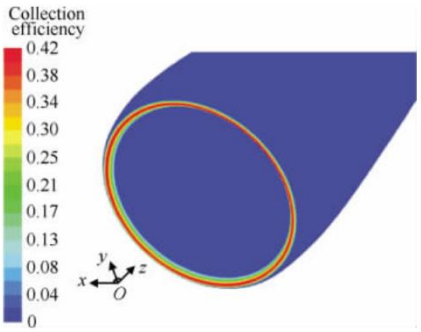


Fig.9 Collection efficiency of local water

Figure 10 shows the prediction results of engine ice shape under Case1 and Case2. In Case2, the temperature is higher, water droplets will not freeze immediately after hitting the wall, some water will overflow

to the rear, so the icing range in Case2 is larger than Case1.

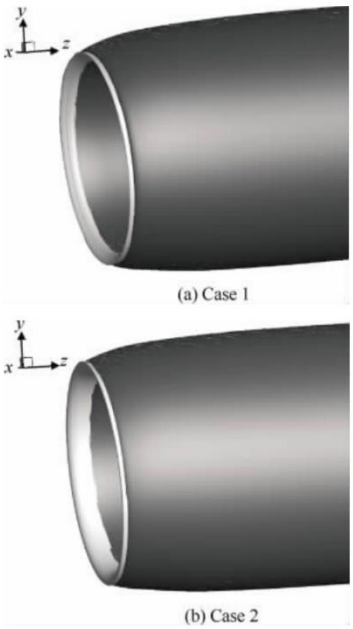


Fig.10 Computational results of engine ice shape

From the above experimental results, it can be seen that the skin temperature of the diversion baffle is higher than zero degrees Celsius under all experimental conditions. When the supercooled water droplets impact on the skin of the disease-proof area, they evaporate and do not flow outside the ice-proof area. The above situation shows that the proposed method can effectively analyze not only the ice-proof power of the aircraft engine inlet, but also the ice-proof performance of the diversion baffle.

According to the above experimental results, it can be seen that the proposed method can better model the anti-icing capability of aircraft engine intake, with smaller overall error.

## 4 Discussions

The so-called aircraft icing is in flight, some parts of the aircraft sometimes appear because of the freezing of water droplets or the accumulation of water vapor condensation ice. When an aircraft encounters ice crystal clouds, dry icing will be produced; condensation icing will be produced when it encounters water vapor; and droplet icing will be produced when it encounters supercooled water droplets. Droplet icing is the most common form of icing.

The process of aircraft icing can be addressed by two systems: one is anti-icing system, which does not allow icing on aircraft components; another type is called deicing system, which allows a small amount of ice to form on aircraft components and then periodically removes the ice. According to the different energy modes used in anti-icing/deicing, there are mechanical anti-icing system, liquid anti-icing system, electrothermal anti-icing/deicing system, gas-thermal anti-icing/deicing system and so on.

1. Mechanical deicing system

The ice is broken mechanically and then blown out by air or removed by centrifugal force and vibration. There are many mechanical methods to break ice, such as using rubber tube inflation to break ice, using ultrasound to deicing the high frequency vibration of skin, or periodically giving a pulse force to the skin to produce high frequency vibration and deicing. Mechanical deicing is widely used in early low-speed aircraft.

2. Liquid anti-icing system

This system continuously supplies anti-icing liquid to the anti-icing surface. The anti-icing liquid is mixed with the water of the mobile phone, which makes the freezing point of the mixed liquid lower than the surface temperature. Anti-icing liquid includes ethylene glycol, isopropanol, ethanol and so on.

3. Gas-thermal anti-icing system

Hot air from engine compressor is often adopted to prevent icing. After the hot air from the engine compressor enters the anti-icing chamber, heat is transferred to the skin during the flow process, so that the temperature of the anti-icing surface reaches a certain value, thus ensuring that the surface does not freeze.

4. Electrothermalanti-icing/deicing system

Electric heating is mainly used to heat the anti-icing surface in order to achieve anti-icing or de-icing effect. The surface continuous electric heating anti-icing system will consume a lot of electric energy for the parts of aircraft wing, tail wing and helicopter rotor. Generally, the periodic electric deicing system is used.

Based on the requirement of Civil Aeroengine Design and airworthiness Conformity verification in our country at present, the following aspects should be attached with attention in model development:

1. The design of anti-icing system for civil aero-engine intake port has just started in China. The requirements of airworthiness clauses and the corresponding airworthiness Conformity verification methods need to be further studied to establish a domestic airworthiness Conformity verification system for anti-icing design of civil aero-engine intake port.

2. The numerical simulation of inlet anti-icing design usually adopts decoupling method, which is affected by simulation accuracy. Most of the design optimization and verification of anti-icing system need to be verified in the ice wind tunnel. The construction of domestic ice wind tunnel test capacity needs to be further developed. Taking engineering design requirements as traction, the test capability of ice wind tunnel is improved.

3. Ice wind tunnel test verification of Civil Aeroengine intake anti-icing system has been developed maturely in foreign countries. Domestic ice wind tunnel test technology and system design verification technology of anti-icing system have just started in recent years. Some newly built hardware equipment of domestic ice wind tunnel has been available, and the parameters of ice cloud and fog are being debugged. Follow-up studies need to be based on the process of icing and anti-icing. According to the requirements of similar test process, the design technology of test model and test measurement technology are further explored.

## 5 Conclusions

The anti-ice performance of engine intake directly affects the operation safety of aircraft. This paper studies the modeling and analysis of the anti-ice ability of engine intake based on symmetry algorithm. Based on the flow field of the intake port of the aircraft engine, the anti-ice ability of the intake port of the aircraft engine is effectively analyzed by using the symmetrical particle swarm optimization algorithm. The proposed method can effectively analyze the anti-ice power of the engine inlet. When the number of iterations of the anti ice power of the engine inlet is less than 1000, the absolute error of the calculation is less than 1%, and the absolute error of the anti ice power of the engine inlet is more than 1.5%, indicating faster calculation speed and the more accurate calculation results of power rate. However, the effectiveness of method proposed needs to be further verified based on more practical simulations and more actual data.

## References

1. Yang Q , Guo Z , Zheng M , et al.(2019) The Effect of Crosswinds on Icing at Turbofan Engine Inlet[C]// International Conference on Icing of Aircraft, Engines, and Structures.
2. Wei, G.W., Guang, Z.G., (2019). Liquid infused surfaces with anti-icing properties. Nanoscale 11(2):159-164.
3. Vercillo V , Karpen N , Laroche A , et al.(2019) Analysis and modelling of icing of air intake protection grids of aircraft engines[J]. Cold Regions Science and Technology,160(APR.):265-272.
4. Weston D . (2018)Vestas launches electrothermal anti-ice system[J]. Windpower Monthly, 34(3):10-10.
5. Zheng M , Guo Z , Dong W , et al.(2019) Experimental investigation on ice accretion on a rotating aero-engine spinner with hydrophobic coating[J]. International Journal of Heat and Mass Transfer,136(JUN.):404-414.
6. Porter C .(2019) Predicted Ice Shape Formations on a Boundary Layer Ingesting Engine Inlet[C]// International Conference on Icing of Aircraft, Engines, and Structures.
7. Lin A , Zhou J , Fawzy H , et al.(2019) Evaluation of mass injection cooling on flow and heat transfer characteristics for high-temperature inlet air in a MIPCC engine[J].

International Journal of Heat and Mass Transfer, 135(JUN.):620-630.
8. Han Y , Soltis J , Palacios J .(2018) Engine Inlet Guide Vane Ice Impact Fragmentation[J]. Aiaa Journal, 56(9):3680-3690.
9. Agureev I E , Elagin M Y , Pavlov D V , et al.(2020) Studies of the process of heating air in the inlet pipe for starting a diesel engine at low temperatures[J]. IOP Conference Series: Materials Science and Engineering, 971(4):042028 (5pp).
10. Moser R , Roberts I .(2019) Numerical Optimisation of a Helicopter Engine Inlet Electrothermal Ice Protection System[C]// International Conference on Icing of Aircraft, Engines, and Structures.
11. Lee J W , Cho M Y , Kim Y H , et al. (2020)Current Status and Prospect of Aircraft Ice Protection Systems[J]. Journal of the Korean Society for Aeronautical & Space Sciences, 48(11):911-925.
12. Son, C., Yee, K. (2017). Procedure for Determining Operation Limits of High-Altitude Long-Endurance Aircraft Under Icing Conditions. Journal of Aircraft 55(2):1-16.
13. Stankowski, T. P., Macmanus, D. G. & Robinson, M. (2017).Aerodynamic Effects of Propulsion Integration for High Bypass Ratio Engines. Journal of Aircraft 54(14):1-15.
14. Xi, C., Zhao, Q. J. (2017).Numerical Simulations for Ice Accretion on Rotors Using New Three-Dimensional Icing Model. Journal of Aircraft 54(4):1-15.
15. Yang, L., Bond, L.J. &Hui, H. (2017).Ultrasonic-Attenuation-Based Technique for Ice Characterization Pertinent to Aircraft Icing Phenomena.Aiaa Journal 55(5):1-8.
16. Synylo K , Krupko A , Zaporozhets O , et al.(2020) CFD simulation of exhaust gases jet from aircraft engine[J]. Energy, 118610.
17. Ma, Yuan, Han, et al.(2019) Improved Chaotic Particle Swarm Optimization Algorithm with More Symmetric Distribution for Numerical Function Optimization[J]. Symmetry, 11(7):876.
18. Sinuo L , Xiaojuan B , Ben W , et al.(2018) A Symmetric Particle-Based Simulation Scheme towards Large Scale Diffuse Fluids[J]. Symmetry, 10(4):86.
19. A. Jakovác, A. Patkós.(2020) Interacting two-particle states in the symmetric phase of the chiral Nambu–Jona-Lasinio model[J]. Modern Physics Letters A, 2050130.
20. Liu H , Liu Y , Zhen J .(2020) Study on inertia weight decreasing strategy of particle swarm optimization based on inverse coseca[J]. Journal of Physics Conference Series, 1486:072004.